

STANDING SAUSAGE MODES IN NONUNIFORM MAGNETIC TUBES: AN INVERSION SCHEME FOR INFERRING FLARE LOOP PARAMETERS

Shao-Xia Chen¹

Bo Li¹

bb1@sdu.edu.cn

Ming Xiong²

Hui Yu¹

and

Ming-Zhe Guo¹

ABSTRACT

Standing sausage modes in flare loops are important for interpreting quasi-periodic pulsations (QPPs) in solar flare lightcurves. We propose an inversion scheme that consistently uses their periods P and damping times τ to diagnose flare loop parameters. We derive a generic dispersion relation governing linear sausage waves in pressure-less straight tubes, for which the transverse density inhomogeneity takes place in a layer of arbitrary width l and is of arbitrary form. We find that P and τ depend on the combination of $[R/v_{Ai}, L/R, l/R, \rho_i/\rho_e]$, where R is the loop radius, L is the looplenth, v_{Ai} is the internal Alfvén speed, and ρ_i/ρ_e is the density contrast. For all the density profiles examined, P and τ experience saturation when $L/R \gg 1$, yielding an inversion curve in the $[R/v_{Ai}, l/R, \rho_i/\rho_e]$ space with a specific density profile when L/R is sufficiently large. When applied to a spatially unresolved QPP event, the scheme yields that R/v_{Ai} is the best constrained, whereas l/R corresponds to the other extreme. For spatially resolved QPPs, while $L/R \gg 1$ cannot be assumed beforehand, an inversion curve remains possible due to additional geometrical constraints. When

¹Shandong Provincial Key Laboratory of Optical Astronomy and Solar-Terrestrial Environment, Institute of Space Sciences, Shandong University, Weihai, 264209, China

²National Space Science Center, CAS, 100190 Beijing, China

a spatially resolved QPP event involves another mode, as is the case for a recent event, the full set of $[v_{Ai}, l, \rho_i/\rho_e]$ can be inferred. We conclude that the proposed scheme provides a useful tool for magneto-seismologically exploiting QPPs.

Subject headings: magnetohydrodynamics (MHD) — Sun: flares — Sun: corona — Sun: magnetic fields — waves

1. INTRODUCTION

The original ideas that laid the foundation for the field of solar magneto-seismology (SMS) were put forward in the 1970s (Uchida 1970, Rosenberg 1970, Zaitsev & Stepanov 1975, see also Roberts et al. 1984). However, this field flourished only after a rich variety of low-frequency Magnetohydrodynamic (MHD) waves and oscillations were identified with the advent of the TRACE, SOHO, Hinode, and SDO satellites (for recent reviews, see Banerjee et al. 2007, De Moortel & Nakariakov 2012, Mathioudakis et al. 2013; and also Ballester et al. 2007, Nakariakov & Erdélyi 2009, Erdélyi & Goossens 2011 for three recent topical issues). It is also indispensable to refine the theoretical understanding of the collective wave modes supported by magnetized tubes, thereby enabling one to employ the measured wave properties to infer the solar atmospheric parameters that are difficult to measure directly (e.g., Roberts 2000; Nakariakov & Verwichte 2005). Regarding its applications to the solar corona, SMS can offer such key information as the magnetic field strength in coronal loops (e.g., Nakariakov & Ofman 2001; Erdélyi & Taroyan 2008; Ofman & Wang 2008; White & Verwichte 2012) and above streamer stalks (Chen et al. 2010, 2011), the magnitude of field-aligned loop flows (Li et al. 2013; Chen et al. 2014), the temperature of loop plasmas (e.g., Marsh & Walsh 2009), the coronal effective adiabatic index (Van Doorsselaere et al. 2011), as well as the longitudinal (Verth & Erdélyi 2008; Andries et al. 2009; Luna-Cardozo et al. 2012a) and transverse structuring (e.g., Arregui et al. 2007; Goossens et al. 2008; Yuan et al. 2015). In addition, SMS applications with torsional Alfvén waves have proven invaluable in inferring the magnetic field structure at chromospheric heights (Jess et al. 2009; Fedun et al. 2011). Likewise, Luna-Cardozo et al. (2012a) demonstrated the potential of using longitudinal waves to infer the longitudinal variation of density and magnetic field strength in chromospheric waveguides.

Magneto-seismological applications with standing kink modes (with azimuthal wavenumber $m = 1$) have been a common practice since their detection with TRACE (Aschwanden et al. 1999). Kink oscillations tend to experience substantial damping (e.g., Ofman & Aschwanden 2002; Ruderman & Erdélyi 2009; Verwichte et al. 2013, and references therein), which is usually interpreted in terms of resonant absorption (Ruderman & Roberts 2002,

Goossens et al. 2002, also Hollweg & Yang 1988, and the comprehensive review by Goossens et al. 2011). With this interpretation, Ruderman & Roberts (2002) and Goossens et al. (2002) suggested that the measured period P and damping time τ can be used to infer the lengthscale l of the density inhomogeneity across coronal loops in units of loop radius R . For this purpose, the largely unknown transverse density distribution was shown to be important, since its formulation has a considerable impact on P and τ (Soler et al. 2013, 2014).

While kink modes have attracted much attention, sausage modes (with $m = 0$) are equally important in SMS. In fact, sausage modes are even more important from the stand-point of solar atmospheric heating given their stronger compressibility and ubiquity in the lower solar atmosphere (Morton et al. 2011, 2012; Freij et al. 2014; Dorotović et al. 2014; Grant et al. 2015; Moreels et al. 2015). In addition, sausage modes are important for interpreting quasi-periodic pulsations (QPPs) in the lightcurves of solar flares (see Nakariakov & Melnikov 2009, for a recent review). Two distinct regimes are known to exist, depending on the axial wavenumber k along flare loops (Nakariakov & Verwichte 2005). The trapped regime results when k exceeds some critical value k_c , where the energy of sausage modes is well confined to magnetic tubes. When $k < k_c$, the leaky regime arises and sausage modes experience apparent temporal damping by radiating their energy into the surrounding fluid (Spruit 1982; Cally 1986). It is known that k_c depends sensitively on the density contrast between loops and their surroundings (e.g., Kopylova et al. 2007). In addition, both eigen-mode analyses (Kopylova et al. 2007; Vasheghani Farahani et al. 2014) and numerical simulations from an initial-value-problem perspective (Nakariakov et al. 2012; Chen et al. 2015) indicated that the period P of sausage modes increases smoothly with decreasing k (or equivalently with increasing looplength L given that $k = \pi/L$ for fundamental modes) until reaching some saturation value P_s for sufficiently thin loops ($R/L \ll 1$). Likewise, identically infinite in the trapped regime for ideal MHD fluids, the attenuation time τ decreases with decreasing k before experiencing saturation at τ_s when $R/L \ll 1$.

Magneto-seismological applications of sausage modes are possible due to their dependence on atmospheric parameters (Luna-Cardozo et al. 2012a,b). The practice based on the measured period and damping time can be illustrated by the study presented in Kopylova et al. (2007) where a step-function (top-hat) form was adopted for the transverse density distribution. The saturation values, P_s and τ_s/P_s , for large density contrasts are approximately

$$P_s \approx 2.62 \frac{R}{v_{Ai}}, \quad \frac{\tau_s}{P_s} \approx \frac{1}{\pi^2} \frac{\rho_i}{\rho_e}. \quad (1)$$

As an example, Kopylova et al. (2007) examined the QPP in the radio emissions reported in McLean & Sheridan (1973), where P and τ/P were found to be ~ 4.3 secs and ~ 10 ,

respectively. With the damping attributed to wave leakage, Eq. (1) then yields a density contrast ρ_i/ρ_e of ~ 100 , and a transverse Alfvén transit time R/v_{Ai} of ~ 1.64 secs, provided that the flaring loop in question is sufficiently thin. However, the dependence of P and τ on loop parameters is substantially more involved if one goes a step closer to reality by replacing a step-function density profile with a smooth one. Even for thin loops where neither P nor τ depends on looplenth, both P_s (Nakariakov et al. 2012) and τ_s (Chen et al. 2015) may be sensitive to the steepness, or equivalently the lengthscale, of the transverse density distribution. In mathematical terms, this means that for a given density profile,

$$\begin{aligned} P_s &= \frac{R}{v_{Ai}} F \left(\frac{l}{R}, \frac{\rho_i}{\rho_e} \right), \\ \frac{\tau_s}{P_s} &= G \left(\frac{l}{R}, \frac{\rho_i}{\rho_e} \right). \end{aligned} \quad (2)$$

When only P_s and τ_s are known as is the case for measurements without imaging capabilities, the appearance of l/R no longer allows a unique pair of $[\rho_i/\rho_e, R/v_{Ai}]$ to be deduced. Despite this, one can still constrain the combination $[R/v_{Ai}, \rho_i/\rho_e, l/R]$ by developing a scheme in much the same way that kink modes were employed (Arregui et al. 2007; Goossens et al. 2008; Soler et al. 2014), the only difference being that the transverse Alfvén time R/v_{Ai} replaces the longitudinal one L/v_{Ai} .

The present study aims to develop the aforementioned scheme employing measured periods and damping times of standing sausage modes. An essential ingredient will be to establish the functions F and G in Eq. (2). To this end, we will derive an analytical dispersion relation (DR) governing linear sausage waves hosted by magnetized tubes with a rather general transverse density distribution. The only requirement here is that this density distribution can be decomposed into a uniform cord, a uniform external medium, and a transition layer connecting the two. However, the density distribution in the transition layer is allowed to be arbitrary, thereby making the DR applicable to a rich variety of density profiles. We note that this kind of density profiles has been extensively adopted in kink mode studies (e.g., Soler et al. 2014, and references therein). We further note that developing an analytical DR is important in its own right. Apart from the step-function profile (e.g., Spruit 1982; Cally 1986), analytical DRs in the cylindrical case are available only for a limited set of density profiles (Edwin & Roberts 1986, 1988; Lopin & Nagorny 2014).

This manuscript is organized as follows. Section 2 presents the derivation of the DR and our solution method. A parameter study is presented in Sect. 3 to examine how the period and damping time of sausage modes depend on tube parameters, thereby establishing our numerical scheme for inverting measurements of spatially unresolved QPPs. An extension to spatially resolved QPPs is then given in Sect. 4. Finally, Sect. 5 closes this manuscript with our summary and some concluding remarks.

2. MATHEMATICAL FORMULATION

2.1. Description for the Equilibrium Tube

We consider sausage waves in a structured corona modeled by a density-enhanced cylinder with radius R aligned with a uniform magnetic field $\mathbf{B} = B\hat{z}$, where a cylindrical coordinate system (r, θ, z) is adopted. The equilibrium density is assumed to be a function of r only and of the form

$$\rho(r) = \begin{cases} \rho_i, & 0 \leq r \leq r_i = R - l/2, \\ \rho_{tr}(r), & r_i \leq r \leq r_e = R + l/2, \\ \rho_e, & r \geq r_e. \end{cases} \quad (3)$$

The profile between $[r_i, r_e]$ is such that the equilibrium density ρ decreases continuously from the internal value ρ_i to the external one ρ_e . The thickness of this transition layer, denoted by l , is bounded by 0 and $2R$. The former represents the steepest profile of a step-function form, whereas the latter corresponds to the least steep case.

While our analysis is valid for arbitrary prescriptions of ρ_{tr} , a number of choices have to be made to evaluate quantitatively the effects of equilibrium density profiles. To this end, we select the following profiles,

$$\rho_{tr}(r) = \begin{cases} \rho_i - \frac{\rho_i - \rho_e}{l} \left(r - R + \frac{l}{2} \right), & \text{linear,} \\ \rho_i - \frac{\rho_i - \rho_e}{l^2} \left(r - R + \frac{l}{2} \right)^2, & \text{parabolic,} \\ \rho_e - \frac{\rho_e - \rho_i}{l^2} \left(r - R - \frac{l}{2} \right)^2, & \text{inverse-parabolic,} \\ \frac{\rho_i}{2} \left[\left(1 + \frac{\rho_e}{\rho_i} \right) - \left(1 - \frac{\rho_e}{\rho_i} \right) \sin \frac{\pi(r - R)}{l} \right], & \text{sine.} \end{cases} \quad (4)$$

The profiles labeled linear, parabolic and sine have been examined in substantial detail in the context of standing kink modes (Soler et al. 2013, 2014). An additional profile, labeled inverse-parabolic, is added to make the list more comprehensive in that it naturally complements the parabolic one. Figure 1 illustrates the r -dependence of the chosen equilibrium density profiles. For illustration purposes, ρ_i/ρ_e is chosen to be 100, and l/R is chosen to be unity.

2.2. Solutions for Radial Lagrangian Displacement and Total Pressure Perturbation

Appropriate for the solar corona, we work in the framework of cold (zero- β) MHD, in which case sausage waves do not perturb the z -component of the plasma velocity. Let δv_r denote the radial velocity perturbation, and let δb_r and δb_z denote the radial and longitudinal components of the perturbed magnetic field $\delta\mathbf{b}$, respectively. The perturbed total pressure is then $\delta p_{\text{tot}} = \mathbf{B} \cdot \delta\mathbf{b}/4\pi = B\delta b_z/4\pi$ given the absence of thermal pressure in the zero- β limit. Fourier-decomposing any perturbed value $\delta f(r, z; t)$ as

$$\delta f(r, z; t) = \text{Re} \left\{ \tilde{f}(r) \exp[-i(\omega t - kz)] \right\}, \quad (5)$$

one finds from linearized, ideal, cold MHD equations that

$$\frac{1}{r} \left(r \tilde{\xi}'_r \right)' + \left(\frac{\omega^2}{v_A^2} - k^2 - \frac{1}{r^2} \right) \tilde{\xi}_r = 0, \quad (6)$$

where the prime $' = d/dr$. In addition, $\tilde{\xi}_r = i\tilde{v}_r/\omega$ is the Fourier amplitude of the radial Lagrangian displacement, and $v_A(r) = B/\sqrt{4\pi\rho(r)}$ is the Alfvén speed. The Fourier amplitude of the perturbed total pressure is

$$\tilde{p}_{\text{tot}} = -\frac{B^2}{4\pi r} \left(r \tilde{\xi}_r \right)'. \quad (7)$$

With azimuthal wavenumber m being 0, the equations governing linear sausage waves are free of singularities, making our derivation simpler than in kink mode studies where a treatment of singularity is necessary (Soler et al. 2013). To be specific, the solutions to Eq. (6) in the transition layer can be expressed as a regular series expansion in $x \equiv r - R$. Let $\tilde{\xi}_{\text{tr},1}$ and $\tilde{\xi}_{\text{tr},2}$ denote two independent solutions,

$$\tilde{\xi}_{\text{tr},1}(x) = \sum_{n=0}^{\infty} a_n x^n, \quad \tilde{\xi}_{\text{tr},2}(x) = \sum_{n=0}^{\infty} b_n x^n. \quad (8)$$

Without loss of generality, one may choose $[a_0, a_1] = [R, 0]$ and $[b_0, b_1] = [0, 1]$. Expanding the equilibrium density ρ about $x = 0$ as well, one finds that

$$\rho_{\text{tr}}(x) = \sum_{n=0}^{\infty} \rho_n x^n, \quad (9)$$

with $\rho_0 = \rho|_{x=0}$ and

$$\rho_n = \frac{1}{n!} \left. \frac{d^n \rho(x)}{dx^n} \right|_{x=0}, \quad n \geq 1. \quad (10)$$

Plugging Eq. (8) into Eq. (6) with the change of independent variable from r to x , and then ordering the terms according to powers in x , one finds that

$$\begin{aligned}\chi_2 &= \frac{-1}{2R^2} [R\chi_1 + (\eta\omega^2 R^2 \rho_0 - k^2 R^2 - 1) \chi_0] , \\ \chi_3 &= \frac{-1}{6R^2} [6R\chi_2 + (\eta\omega^2 R^2 \rho_0 - k^2 R^2) \chi_1 \\ &\quad + (\eta\omega^2 R^2 \rho_1 + 2\eta\omega^2 R \rho_0 - 2k^2 R) \chi_0] , \\ \chi_n &= \frac{-1}{n(n-1)R^2} \left\{ (n-1)(2n-3)R\chi_{n-1} + \eta\omega^2 R^2 \sum_{l=0}^{n-2} \rho_{n-l-2} \chi_l \right. \\ &\quad + [(n-3)(n-1) - k^2 R^2] \chi_{n-2} + 2\eta\omega^2 R \sum_{l=0}^{n-3} \rho_{n-l-3} \chi_l \\ &\quad \left. - 2k^2 R \chi_{n-3} - k^2 \chi_{n-4} + \eta\omega^2 \sum_{l=0}^{n-4} \rho_{n-l-4} \chi_l \right\} , \quad (n \geq 4)\end{aligned}\quad (11)$$

where $\eta = 4\pi/B^2$ and χ represents either a or b .

With Eq. (8) at hand, the solution to Eq. (6) can be expressed as

$$\tilde{\xi}_r(r) = \begin{cases} A_i J_1(\mu_i r), & 0 \leq r \leq r_i, \\ A_1 \tilde{\xi}_{tr,1}(x) + A_2 \tilde{\xi}_{tr,2}(x), & r_i \leq r \leq r_e, \\ A_e H_1^{(1)}(\mu_e r), & r \geq r_e, \end{cases} \quad (12)$$

where A_i, A_e, A_1 and A_2 are arbitrary constants, and J_n and $H_n^{(1)}$ are the n -th-order Bessel and Hankel functions of the first kind, respectively (here $n = 1$). In addition, $\mu_{i,e}^2 = \omega^2/v_{Ai,e}^2 - k^2$ with $v_{Ai,e}^2 = B^2/(4\pi\rho_{i,e})$. As discussed in Cally (1986), requiring that $-\pi/2 < \arg \mu_i, \arg \mu_e \leq \pi/2$ does not exclude any additional independent solution. Furthermore, expressing the external solution in terms of $H_n^{(1)}$ permits a unified examination of both trapped and leaky waves. Indeed, the trapped regime arises when $\arg \mu_e = \pi/2$, in which case one finds that $H_1^{(1)}(\mu_e r) = -(2/\pi)K_1(\alpha r)$ with $\alpha = \mu_e/i$ being real and positive (see discussions on page 281 in Cally 1986). Now the Fourier amplitude for the total pressure perturbation can be evaluated with Eq. (7), the results being

$$\tilde{p}_{\text{tot}}(r) = \begin{cases} -\frac{A_i B^2}{4\pi} \mu_i J_0(\mu_i r) , & 0 \leq r \leq r_i, \\ -\frac{B^2}{4\pi r} \left\{ A_1 \frac{d}{dx} [(x+R) \tilde{\xi}_{tr,1}(x)] + A_2 \frac{d}{dx} [(x+R) \tilde{\xi}_{tr,2}(x)] \right\} , & r_i \leq r \leq r_e \\ -\frac{A_e B^2}{4\pi} \mu_e H_0^{(1)}(\mu_e r) , & r \geq r_e, \end{cases} \quad (13)$$

The expression for \tilde{p}_{tot} for the ranges $r \leq r_i$ and $r \geq r_e$ can also be independently verified by using an alternative relation between $\tilde{\xi}_r$ and \tilde{p}_{tot} ,

$$\tilde{\xi}_r = \frac{d\tilde{p}_{\text{tot}}/dr}{\rho(\omega^2 - k^2 v_A^2)} .$$

2.3. Dispersion Relation of Sausage Waves

The dispersion relation (DR) governing linear sausage waves can be derived by requiring that both $\tilde{\xi}_r$ and \tilde{p}_{tot} be continuous at the interfaces $r = r_i$ and $r = r_e$. This leads to

$$\begin{aligned} A_i J_1(\mu_i r_i) &= A_1 \tilde{\xi}_{\text{tr},1}(x_i) + A_2 \tilde{\xi}_{\text{tr},2}(x_i), \\ A_e H_1^{(1)}(\mu_e r_e) &= A_1 \tilde{\xi}_{\text{tr},1}(x_e) + A_2 \tilde{\xi}_{\text{tr},2}(x_e), \\ A_i \mu_i r_i J_0(\mu_i r_i) &= [A_1 \tilde{\xi}_{\text{tr},1}(x_i) + A_2 \tilde{\xi}_{\text{tr},2}(x_i)] + r_i [A_1 \tilde{\xi}'_{\text{tr},1}(x_i) + A_2 \tilde{\xi}'_{\text{tr},2}(x_i)], \\ A_e \mu_e r_e H_0^{(1)}(\mu_e r_e) &= [A_1 \tilde{\xi}_{\text{tr},1}(x_e) + A_2 \tilde{\xi}_{\text{tr},2}(x_e)] + r_e [A_1 \tilde{\xi}'_{\text{tr},1}(x_e) + A_2 \tilde{\xi}'_{\text{tr},2}(x_e)], \end{aligned}$$

where $x_i = -l/2$ and $x_e = l/2$. Eliminating A_i (A_e) by dividing the third (fourth) by the first (second) equation, one finds that

$$\begin{aligned} \Lambda_1 A_1 + \Lambda_2 A_2 &= 0, \\ \Lambda_3 A_1 + \Lambda_4 A_2 &= 0, \end{aligned} \tag{14}$$

where the coefficients read

$$\begin{aligned} \Lambda_1 &= \tilde{\xi}_{\text{tr},1}(x_i) + r_i \tilde{\xi}'_{\text{tr},1}(x_i) - X_i \tilde{\xi}_{\text{tr},1}(x_i), \\ \Lambda_2 &= \tilde{\xi}_{\text{tr},2}(x_i) + r_i \tilde{\xi}'_{\text{tr},2}(x_i) - X_i \tilde{\xi}_{\text{tr},2}(x_i), \\ \Lambda_3 &= \tilde{\xi}_{\text{tr},1}(x_e) + r_e \tilde{\xi}'_{\text{tr},1}(x_e) - X_e \tilde{\xi}_{\text{tr},1}(x_e), \\ \Lambda_4 &= \tilde{\xi}_{\text{tr},2}(x_e) + r_e \tilde{\xi}'_{\text{tr},2}(x_e) - X_e \tilde{\xi}_{\text{tr},2}(x_e), \end{aligned} \tag{15}$$

with

$$\begin{aligned} X_i &= \frac{\mu_i r_i J_0(\mu_i r_i)}{J_1(\mu_i r_i)}, \\ X_e &= \frac{\mu_e r_e H_0^{(1)}(\mu_e r_e)}{H_1^{(1)}(\mu_e r_e)}. \end{aligned} \tag{16}$$

Evidently, for Eq. (14) to allow non-trivial solutions of $[A_1, A_2]$, one needs to require that

$$\Lambda_1 \Lambda_4 - \Lambda_2 \Lambda_3 = 0, \tag{17}$$

which is the DR governing sausage waves in nonuniform loops.

Does Eq. (17), the DR valid for arbitrary l/R , recover the well-known result for the step-function profile when $l/R \rightarrow 0$? Retaining only terms to the 0-th order in l/R and noting that $r_i \approx r_e \approx R$, one finds that Λ_n ($n = 1, \dots, 4$) simplify to

$$\begin{aligned}\Lambda_1 &= (1 - X_i)a_0 + Ra_1, \\ \Lambda_2 &= (1 - X_i)b_0 + Rb_1, \\ \Lambda_3 &= (1 - X_e)a_0 + Ra_1, \\ \Lambda_4 &= (1 - X_e)b_0 + Rb_1.\end{aligned}$$

Substituting these expressions into Eq. (17), one finds that

$$(X_i - X_e)(a_1b_0 - a_0b_1) = 0.$$

This leads to $X_i = X_e$, given that $a_1b_0 - a_0b_1$ is not allowed to be zero for $\tilde{\xi}_{tr,1}$ and $\tilde{\xi}_{tr,2}$ to be independent. In other words (see Eq. (16))

$$\frac{\mu_i J_0(\mu_i R)}{J_1(\mu_i R)} = \frac{\mu_e H_0^{(1)}(\mu_e R)}{H_1^{(1)}(\mu_e R)}, \quad (18)$$

which is the DR for equilibrium density profiles of a step-function form (e.g., [Cally 1986](#)).

While the DR is equally applicable to propagating waves, we will focus on standing modes for which the axial wavenumber k is real, while the angular frequency ω is allowed to be complex-valued. Furthermore, let us focus on fundamental standing modes supported by magnetized tubes of length L . In this case, another measure to validate the DR, independent of the eigen-value problem approach, is to employ the linearized, time-dependent, cold MHD equations to derive an equation governing the transverse velocity perturbation $v_r(r, z, t)$. In view of the line-tying boundary conditions at the loop ends $z = 0$ and $z = L$, one may express $v_r(r, z, t)$ as $v(r, t) \sin(kz)$ with $k = \pi/L$, yielding ([Nakariakov et al. 2012](#); [Chen et al. 2015](#))

$$\frac{\partial^2 v(r, t)}{\partial t^2} = v_A^2(r) \left[\frac{\partial^2}{\partial r^2} + \frac{1}{r} \frac{\partial}{\partial r} - \left(k^2 + \frac{1}{r^2} \right) \right] v(r, t). \quad (19)$$

When supplemented with appropriate boundary and initial conditions, the signal of $v_r(r, t)$ at some arbitrarily chosen distance from the tube axis can be followed. As demonstrated in [Nakariakov et al. \(2012\)](#); [Chen et al. \(2015\)](#), after a transitory phase this signal evolves into a harmonic (decaying harmonic) form when k is larger (less) than some critical value, corresponding to the well-known trapped (leaky) regime. Numerically fitting the signal with a sinusoidal (exponentially decaying sinusoidal) function then yields the period P (P together with the damping time τ) for trapped (leaky) modes. We also adopt this approach and compare the derived values for P and τ with what is found by solving the DR for

complex-valued ω at given real k . As will be shown in Fig. 2, the two sets of independently derived values for $[P, \tau]$ agree remarkably well. At this point, it should be remarked that once a choice for ρ_{tr} is made, P and τ depend only on the combination of parameters $[\rho_i/\rho_e, l/R, L/R]$ when they are measured in units of the internal Alfvén transit time R/v_{Ai} . Here we have used $L/R = \pi/(kR)$ in place of the dimensionless axial wavenumber kR .

In general, the DR (Eq. (17)) is not analytically tractable and is solved numerically for a given ρ_{tr} profile and some given combination of $[\rho_i/\rho_e, l/R, L/R]$. To do so requires the infinite series expansion in Eq.(8) to be truncated by retaining the terms with n up to a certain N . A value of $N = 101$ is chosen for all the numerical results to be presented, and we have made sure that using an even larger N does not introduce any appreciable difference. In addition, we focus only on the lowest order modes, namely those with the simplest radial structure in the eigen-functions. When verifying these results with the computations from an initial-value-problem perspective, we choose not to use a too localized initial perturbation $v(r, t = 0)$ (see Eq.(19)), otherwise higher order modes are introduced to contaminate the $v(r, t)$ signals.

3. NUMERICAL RESULTS AND THE INVERSION SCHEME

Let us start with an examination of how the ρ_{tr} profile impacts the dispersive properties of standing sausage modes. Figure 2 shows the dependence on the length-to-radius ratio L/R of the period P and damping time τ for different choices of $\rho_{\text{tr}}(r)$ as labeled. For illustration purposes, we choose the density contrast ρ_i/ρ_e to be 100, and choose l/R to be unity. The black line in Fig. 2a, which represents $2L/v_{\text{Ae}}$, separates the trapped (to its left, where τ is identically infinite) from leaky (to its right) regimes. The curves are found by solving the analytical DR (Eq. (17)), whereas the open circles are found by solving the corresponding time-dependent equation (see Eq. (19) and the associated description). Evidently, the periods P and damping times τ obtained from the two independent approaches agree with each other remarkably well. Figure 2 indicates that the overall tendency for P (τ) to increase (decrease) with L/R is seen for all the equilibrium density profiles considered. In particular, regardless of the profiles, both P and τ tend to some asymptotic values at large L/R . However, the choice of equilibrium density profiles has a considerable influence on the specific values for P and τ . This is particularly true if one compares the results for the parabolic and inverse-parabolic profiles, given by the green and blue curves, respectively. Furthermore, while the periods P for the linear and sine profiles differ little for the chosen l/R , the damping times τ show a stronger profile dependence. This signifies the importance of using P and τ in a consistent manner when one attempts to deduce how the transverse

equilibrium density is structured.

The effects of equilibrium density profile can be better brought out by capitalizing on the fact that both P and τ experience saturation for sufficiently thin loops. Let P_s and τ_s denote the saturation values. Figure 3 presents how P_s and τ_s/P_s depend on l/R , the width of the transition layer in units of loop radius. The density contrast is chosen to be 100, and different choices of ρ_{tr} are represented by the curves in different colors as labeled in Fig. 3b. In addition, in place of τ_s , the ratio τ_s/P_s is plotted since it is a better measure of signal quality. One sees from Figs. 3a and 3b that the curves converge at $l/R \rightarrow 0$ as expected given that the DR (Eq. (17)) simplifies to Eq. (18) pertinent to a top-hat density distribution. Figure 3a indicates that the l/R -dependence of P_s critically depends on how ρ_{tr} is described. For the parabolic profile, P_s increases monotonically with l/R , whereas the opposite trend is found for the inverse-parabolic profile. When it comes to the linear and sine profiles, Fig. 3a shows that the l/R -dependence of P_s is not as strong, and the difference between the two profiles is discernible only when $l/R \gtrsim 1$. Moving on to Fig. 3b, one sees that the ratio τ_s/P_s decreases monotonically with l/R for all the profiles, meaning that wave leakage plays an increasingly important role in attenuating sausage modes when the loop becomes more diffuse. Reinforcing the impression from Fig. 2b, one sees that relative to P_s , τ_s/P_s better discriminates the equilibrium density profiles.

So far we have fixed the density contrast ρ_i/ρ_e at 100. One naturally asks what happens if ρ_i/ρ_e is varied? Figure 4 presents the distribution of P_s (the left column) and τ_s/P_s (right) in the $[\rho_i/\rho_e, l/R]$ plane. Each row represents one of the four density profiles as labeled. Besides, the red curve represents where $\tau_s/P_s = 10$, the value for the QPP event reported in [McLean & Sheridan \(1973\)](#). Examine the left column first. One sees from Figs. 4b and 4c that in the parameter range examined, P_s tends to increase (decrease) with l/R at any given ρ_i/ρ_e when the parabolic (inverse-parabolic) profile is chosen. In contrast, Figs. 4a and 4d indicate that P_s for the linear and sine profiles shows a nonmonotonical dependence on l/R , even though this variation is hardly discernible. Now consider the right column, from which one can see that regardless of the profiles, τ_s/P_s decreases with increasing l/R for all the density contrasts examined. In addition, the dependence of τ_s/P_s on l/R is the strongest for the inverse-parabolic profile, and the least strong for the parabolic one. The dependence for the linear and sine profiles lies in between, with the dependence in the linear case being slightly stronger.

Conceptually, Fig. 4 can be used to invert the measured values of the period and damping time of sausage modes, provided that the loops hosting these oscillations are sufficiently thin. Consider the QPP event reported in [McLean & Sheridan \(1973\)](#) as an example, for which $P_s = 4.3$ secs and $\tau_s/P_s = 10$. It then follows that for a given density profile, any point

along the corresponding red curve in Fig. 4 can equally reproduce the measured τ_s/P_s . After reading any pair of $[\rho_i/\rho_e, l/R]$, one can read from the left column the corresponding value for P_s in units of R/v_{Ai} . With P_s known, one can then deduce R/v_{Ai} . In practice, however, constructing such a contour plot is not necessary, and one may simply consider the following 3-step inversion scheme. First, one starts with the dispersion relation for a step-function density profile ($l/R = 0$), Eq. (18), to find the value for the density contrast ρ_i/ρ_e such that τ_s/P_s agrees with the measured value. Second, with the ρ_i/ρ_e value for a smaller l/R as a good guess, one can then solve Eq. (17) to find a new ρ_i/ρ_e that yields the measured τ_s/P_s by increasing l/R from 0 to 2 consecutively. Third, with ρ_i/ρ_e found for all possible l/R , one can solve Eq. (17) for a given pair of $[\rho_i/\rho_e, l/R]$, yielding a value for $P_s/(R/v_{Ai})$. Finding the transverse Alfvén transit time R/v_{Ai} is then straightforward since P_s is known.

The product of the inversion scheme is an inversion curve in the three-dimensional (3D) space formed by R/v_{Ai} , l/R and ρ_i/ρ_e . Figure 5 presents such curves (the solid lines) and their projections onto various planes (dashed) for the examined density profiles, pertinent to the event reported in [McLean & Sheridan \(1973\)](#). To help digest this figure, a number of points are read from the curves and presented in Table 1. One sees that among the parameters forming this 3D space, R/v_{Ai} is the best constrained. The biggest (smallest) value, 2.13 (1.18) secs, is found for the inverse-parabolic (parabolic) profile when $l/R \rightarrow 2$. In other words, the biggest value exceeds the smallest one by only 79.7%. As to the density contrast, the biggest value (251.4 found for the inverse-parabolic profile when $l/R \rightarrow 2$) is larger than the smallest one (88.1 when $l/R \rightarrow 0$) by 185%. The least constrained parameter is l/R , with any value in the allowed range from 0 to 2 being possible.

4. FURTHER DEVELOPMENT OF THE INVERSION SCHEME

Before proceeding, let us first recap the key points in the scheme for inverting the measured period P and damping time τ of sausage modes. From the outset, we have assumed that only P and τ are known, whereas we have no information on either the geometric parameters (R , L , and l) or the physical parameters (v_{Ai} , ρ_i , and ρ_e). On top of that, the specific density profile is also assumed to be unknown. This happens when one has only spatially unresolved observations (see e.g., the majority of the events compiled in [Aschwanden et al. 2004](#), Table 1). In this case, the dispersion relation, Eq. (17), suggests that in general

the periods and damping times can be formally expressed as

$$\begin{aligned} P_{\text{saus}} &= \frac{R}{v_{\text{Ai}}} F_{\text{saus}} \left(\frac{L}{R}, \frac{l}{R}, \frac{\rho_i}{\rho_e} \right), \\ \frac{\tau_{\text{saus}}}{P_{\text{saus}}} &= G_{\text{saus}} \left(\frac{L}{R}, \frac{l}{R}, \frac{\rho_i}{\rho_e} \right). \end{aligned} \quad (20)$$

With only two measured values available, any point on a two-dimensional (2D) surface in the four-dimensional (4D) space formed by $[R/v_{\text{Ai}}, L/R, l/R, \rho_i/\rho_e]$ can reproduce the measurements, even if one is allowed to prescribe a density profile. If the sausage modes are in the trapped regime in the sense that the QPPs do not show temporal damping, then the situation becomes even less desired since now the restriction from τ is no longer available. This complexity can be alleviated if the condition $L/R \gg 1$ holds for the flare loops in question since L/R no longer appears such that Eq. (2) is restored. One then finds a curve in the $[R/v_{\text{Ai}}, l/R, \rho_i/\rho_e]$ space as shown by Fig. 5.

The situation improves if the QPP events are spatially resolved, since the looplength (L) and the outer interface of the loops ($r_e = R + l/2$) can be considered known. In this case L/R and l/R are no longer independent but are related by

$$\frac{L}{R} = \frac{L}{r_e} \left(1 + \frac{l}{2R} \right), \quad (21)$$

where we have used the relation

$$R = \frac{2r_e}{2 + l/R}. \quad (22)$$

Now the situation is similar to what Eq. (2) implies: if the sausage mode is a trapped (leaky) one, then a 2D surface (1D curve) can be deduced in the $[R/v_{\text{Ai}}, l/R, \rho_i/\rho_e]$ space. It is just that now for a point on this 2D surface or along the 1D curve, one can further deduce v_{Ai} in view of Eq. (22).

Something fascinating happens if one observes a spatially resolved QPP event hosting more than just a sausage mode. For illustration purposes, we consider the situation where a temporally decaying kink mode is involved, and its damping can be attributed to resonant absorption. In this case, the period and damping time for the kink mode can be formally expressed by

$$\begin{aligned} P_{\text{kink}} &= \frac{L}{v_{\text{Ai}}} F_{\text{kink}} \left(\frac{l}{R}, \frac{\rho_i}{\rho_e} \right), \\ \frac{\tau_{\text{kink}}}{P_{\text{kink}}} &= G_{\text{kink}} \left(\frac{l}{R}, \frac{\rho_i}{\rho_e} \right). \end{aligned} \quad (23)$$

Note that while L/R in principle can be incorporated into Eq. (23), in reality there is no need to do so since the corrections to P_{kink} and τ_{kink} due to finite L/R are of the order $(R/L)^2$ (Van Doorsselaere et al. 2004; Goossens et al. 2008). Even for relatively thick flare loops, R/L is of the order 0.1 and these corrections amount to only a few percent. Note further that F_{kink} and G_{kink} have been extensively studied, and a graphical representation can be found in Fig. 1 of Soler et al. (2014). With F_{kink} , G_{kink} , F_{saus} , and G_{saus} known, it is then possible to fully constrain the unknowns $[l, R, v_{\text{Ai}}, \rho_i/\rho_e]$, if one assumes a density profile. In fact, the measured values of $[P_{\text{kink}}, \tau_{\text{kink}}, P_{\text{saus}}, \tau_{\text{saus}}]$ are more than sufficient: l and R are not independent but are related through Eq. (22). This suggests that only three expressions contained in Eqs. (20) and (23) are needed. In practice, we consider the expression for the kink mode period as the redundant one. Now the inversion procedure is rather straightforward. In view of the relation (21), the two expressions for the damping-time-to-period ratio in Eqs. (20) and Eqs. (23) contain only two unknowns, namely l/R and ρ_i/ρ_e . With both $\tau_{\text{saus}}/P_{\text{saus}}$ and $\tau_{\text{kink}}/P_{\text{kink}}$ available, one can deduce a unique pair of $[l/R, \rho_i/\rho_e]$. The loop radius R then follows from Eq. (22), which then enables one to evaluate v_{Ai} with the first expression in Eq. (20). Finally, as a safety check, one can proceed to evaluate, with the first expression in Eq. (23), the theoretically expected kink mode period $P_{\text{kink, theory}}$. The deviation of $P_{\text{kink, theory}}$ from the measured one then allows to say a few words on how safe it is to identify the oscillation signals with some particular modes.

As an illustration of the aforementioned inversion procedure, let us consider the QPP event in microwave emissions measured with the Nobeyama Radioheliograph (NoRH) on 14 May 2013 (Kolotkov et al. 2015). Lucky enough, it is likely that this event contains a fundamental kink mode with $P_{\text{kink}} = 100$ secs and $\tau_{\text{kink}}/P_{\text{kink}} = 2.5$, in addition to a fundamental sausage mode with $P_{\text{saus}} = 15$ secs and $\tau_{\text{saus}}/P_{\text{saus}} = 6$. Assuming that the apparent width measured therein corresponds to $2r_e$, one finds that $r_e = 4 \times 10^3$ km and $L = 4 \times 10^4$ km, meaning that $L/r_e = 10$. Let us assume that wave leakage is responsible for damping the sausage mode, and resonant absorption is responsible for damping the kink one. Furthermore, let us assume that the sine profile best describes the equilibrium density distribution. In this case, the analytical expressions obtained in the thin-tube-thin-boundary approximation are accurate to within $\sim 25\%$ (e.g., Van Doorsselaere et al. 2004; Soler et al. 2014). This enables us to illustrate our inversion procedure without resorting to a fully numerical solver to establish F_{kink} and G_{kink} . Now the formal expressions given by Eq. (23) can be replaced with (e.g., Goossens et al. 2008)

$$\begin{aligned} P_{\text{kink}} &= \frac{L}{v_{\text{Ai}}} \sqrt{\frac{2(1 + \rho_i/\rho_e)}{\rho_i/\rho_e}}, \\ \frac{\tau_{\text{kink}}}{P_{\text{kink}}} &= \frac{2 \rho_i/\rho_e + 1}{\pi \rho_i/\rho_e - 1} \frac{1}{l/R}. \end{aligned} \tag{24}$$

Following the outlined inversion procedure, we find that $l/R = 0.272$ and $\rho_i/\rho_e = 29.8$ as constrained by the ratios τ/P . It then follows that $R = 3.52 \times 10^3$ km, from which one can deduce that $v_{Ai} = 623$ km s $^{-1}$. Finally, $P_{\text{kink,theory}}$ is found to be 92.2 secs, which agrees with the measured value of 100 secs to within 8%. This safety check lends support to the interpretation of the two modes in terms of fundamental kink and sausage modes as done by [Kolotkov et al. \(2015\)](#). Besides, the deduced Alfvén speed v_{Ai} and density contrast ρ_i/ρ_e both seem reasonable. On top of that, there is no need for one to worry too much about the accuracy of Eq. (24) describing the kink mode: at the deduced $[l/R, \rho_i/\rho_e]$, this equation yields P and τ/P to an accuracy better than 1% and $\sim 6\%$, respectively (see Fig. 1 in [Soler et al. 2014](#)).

5. CONCLUSIONS

How plasma density is structured across various magnetic structures in the solar corona remains largely unknown. It has been a common practice to deduce this key information by employing magneto-seismological techniques that invert the measured period P and damping time τ of standing kink modes collectively supported by a magnetic structure (e.g., [Goossens et al. 2008](#); [Soler et al. 2014](#)). In contrast, while quasi-periodic pulsations (QPPs) in the lightcurves of solar flares are often attributed to standing sausage modes in flare loops and therefore can also offer the associated period and damping time, a scheme is missing for inverting these two measurements to deduce the information on the density distribution transverse to flare loops. The primary aim of this study has been to construct such a scheme. To this end, we worked in the framework of cold (zero- β) MHD and modeled flare loops as straight cylinders with a transverse density profile characterized by a transition layer sandwiched between a uniform cord and a uniform external medium. An analytical dispersion relation (DR) governing linear sausage waves, Eq. (17), was derived by solving the perturbation equations in terms of a regular series expansion in the transition layer. This DR, valid for arbitrary choices of the density profile in the transition layer, then enabled us to examine the effects of density structuring on the periods and damping times of sausage modes, thereby facilitating the construction of the inversion scheme.

In general, we found that P and τ of sausage modes depend on a combination of parameters $[R/v_{Ai}, L/R, l/R, \rho_i/\rho_e]$ as formally expressed by Eq. (20), where the functions F_{saus} and G_{saus} are a product of the DR. Here L and R denote the looplength and loop radius, respectively. Furthermore, l is the width of the transition layer, v_{Ai} is the Alfvén speed in the cord, and ρ_i/ρ_e is the density contrast between the loop and its surrounding fluid. We showed that for the density profiles examined, both P and τ experience saturation for suffi-

ciently large L/R when the rest of the four parameters are fixed. The choice of the transverse density profile was found to have a considerable influence on P and τ , their dependence on l/R in particular.

Our inversion scheme can find applications to both spatially unresolved and resolved QPP events. For spatially unresolved ones, we showed that the best one can do is to deduce a 1D curve in the $[R/v_{Ai}, l/R, \rho_i/\rho_e]$ space for a prescribed density profile. This happens if the QPPs in question experience temporal damping, and if the flare loops hosting them can be assumed to be sufficiently thin. When applied to a QPP event reported by [McLean & Sheridan \(1973\)](#), this inversion technique indicated that the transverse Alfvén transit time R/v_{Ai} is the best constrained, varying by a factor of 80% if the uncertainties in specifying the density profile are taken into account. The density contrast ρ_i/ρ_e is less well constrained, with the largest deduced value exceeding the smallest one by a factor of 1.85. The least constrained is the transverse density lengthscale in units of loop radius (l/R), any value in the allowed range $(0, 2)$ can be equally possible to reproduce the measurements.

When it comes to spatially resolved events, the geometric parameters L and $R+l/2$ are additional constraints, on top of the measured values for P and τ . Even though in this case one cannot assume $L/R \gg 1$ a priori, it is possible to deduce a 1D curve in the $[v_{Ai}, l, \rho_i/\rho_e]$ space for a chosen density profile since R is expressible in terms of l/R . If a spatially resolved QPP event comprises more than just one sausage mode, then it is possible to deduce the full information on $[l, R, v_{Ai}, \rho_i/\rho_e]$. In this case, the inversion problem becomes an over-determined one. We illustrated this fascinating application with the QPP event reported by [Kolotkov et al. \(2015\)](#) where a fundamental kink and a fundamental sausage mode were suggested to co-exist and both experience temporal damping. Attributing the temporal damping of the kink mode to resonant absorption, and that of the sausage mode to wave leakage, we were able to deduce the full set of $[l, R, v_{Ai}, \rho_i/\rho_e]$ by using Eqs. (20) and (24) and assuming a sine profile for the density distribution. One redundant equation, here taken as the expression for the kink mode period, can then allow a safety check on, say, whether it is reasonable to interpret the signals in the QPP event as the aforementioned modes. For this particular event, our results demonstrated that the interpretation provided in [Kolotkov et al. \(2015\)](#) is reasonable, not only because the deduced parameters seem realistic, but also because the theoretical prediction for the kink mode period agrees with the measured one remarkably well.

Our scheme nonetheless has a number of limitations. First, we have assumed that the temporal damping of sausage modes is due to wave leakage, an ideal MHD process. In reality, non-ideal mechanisms like electron heat conduction and ion viscosity can provide additional channels for damping sausage modes. While these non-ideal processes were shown

by Kopylova et al. (2007) to be unlikely the cause for the temporal damping in the QPP event reported by McLean & Sheridan (1973), their importance has yet to be assessed for the event reported by Kolotkov et al. (2015). Second, working in the cold MHD, we have not taken into account the possible effects due to finite plasma beta, which may be of the order unity in flare loops. However, the corrections due to finite beta seem marginal (Inglis et al. 2009). Third, the longitudinal variation in neither the plasma density nor the magnetic field strength has been considered, even though the corrections due to this variation are unlikely to be significant (Pascoe et al. 2009). Fourth, the density inhomogeneity in flare loops was assumed to be in a monolithic form, whereas in reality these loops may be multi-stranded. While the fine structuring in the form of randomly distributed concentric shells is found to have a far less significant influence than the monolithic component of the density distribution (Chen et al. 2015, see also Pascoe et al. 2007), there is a need to rigorously assess the effects due to fine structuring in the form of randomly distributed strands.

We thank the referee for the constructive comments, which helped improve this manuscript substantially. This work is supported by the National Natural Science Foundation of China (41174154, 41274176, and 41474149), and by the Provincial Natural Science Foundation of Shandong via Grant JQ201212.

REFERENCES

Andries, J., van Doorsselaere, T., Roberts, B., Verth, G., Verwichte, E., & Erdélyi, R. 2009, *Space Sci. Rev.*, 149, 3

Arregui, I., Andries, J., Van Doorsselaere, T., Goossens, M., & Poedts, S. 2007, *A&A*, 463, 333

Aschwanden, M. J., Fletcher, L., Schrijver, C. J., & Alexander, D. 1999, *ApJ*, 520, 880

Aschwanden, M. J., Nakariakov, V. M., & Melnikov, V. F. 2004, *ApJ*, 600, 458

Ballester, J. L., Erdélyi, R., Hood, A. W., Leibacher, J. W., & Nakariakov, V. M. 2007, *Sol. Phys.*, 246, 1

Banerjee, D., Erdélyi, R., Oliver, R., & O’Shea, E. 2007, *Sol. Phys.*, 246, 3

Cally, P. S. 1986, *Sol. Phys.*, 103, 277

Chen, S.-X., Li, B., Xia, L.-D., Chen, Y.-J., & Yu, H. 2014, *Sol. Phys.*, 289, 1663

Chen, S.-X., Li, B., Xia, L.-D., & Yu, H. 2015, *Sol. Phys.*

Chen, Y., Feng, S. W., Li, B., Song, H. Q., Xia, L. D., Kong, X. L., & Li, X. 2011, *ApJ*, 728, 147

Chen, Y., Song, H. Q., Li, B., Xia, L. D., Wu, Z., Fu, H., & Li, X. 2010, *ApJ*, 714, 644

De Moortel, I. & Nakariakov, V. M. 2012, *Royal Society of London Philosophical Transactions Series A*, 370, 3193

Dorotovič, I., Erdélyi, R., Freij, N., Karlovský, V., & Márquez, I. 2014, *A&A*, 563, A12

Edwin, P. M. & Roberts, B. 1986, in *NASA Conference Publication*, Vol. 2449, *NASA Conference Publication*, ed. B. R. Dennis, L. E. Orwig, & A. L. Kiplinger, 347–357

Edwin, P. M. & Roberts, B. 1988, *A&A*, 192, 343

Erdélyi, R. & Goossens, M. 2011, *Space Sci. Rev.*, 158, 167

Erdélyi, R. & Taroyan, Y. 2008, *A&A*, 489, L49

Fedun, V., Verth, G., Jess, D. B., & Erdélyi, R. 2011, *ApJ*, 740, L46

Freij, N., Scullion, E. M., Nelson, C. J., Mumford, S., Wedemeyer, S., & Erdélyi, R. 2014, *ApJ*, 791, 61

Goossens, M., Andries, J., & Aschwanden, M. J. 2002, *A&A*, 394, L39

Goossens, M., Arregui, I., Ballester, J. L., & Wang, T. J. 2008, *A&A*, 484, 851

Goossens, M., Erdélyi, R., & Ruderman, M. S. 2011, *Space Sci. Rev.*, 158, 289

Grant, S. D. T., Jess, D. B., Moreels, M. G., Morton, R. J., Christian, D. J., Giagkiozis, I., Verth, G., Fedun, V., Keys, P. H., Van Doorsselaere, T., & Erdélyi, R. 2015, *ApJ*, 806, 132

Hollweg, J. V. & Yang, G. 1988, *J. Geophys. Res.*, 93, 5423

Inglis, A. R., van Doorsselaere, T., Brady, C. S., & Nakariakov, V. M. 2009, *A&A*, 503, 569

Jess, D. B., Mathioudakis, M., Erdélyi, R., Crockett, P. J., Keenan, F. P., & Christian, D. J. 2009, *Science*, 323, 1582

Kolotkov, D. Y., Nakariakov, V. M., Kupriyanova, E. G., Ratcliffe, H., & Shibasaki, K. 2015, *A&A*, 574, A53

Kopylova, Y. G., Melnikov, A. V., Stepanov, A. V., Tsap, Y. T., & Goldvarg, T. B. 2007, *Astronomy Letters*, 33, 706

Li, B., Habbal, S. R., & Chen, Y. 2013, *ApJ*, 767, 169

Lopin, I. & Nagorny, I. 2014, *A&A*, 572, A60

Luna-Cardozo, M., Verth, G., & Erdélyi, R. 2012a, *ApJ*, 748, 110

Luna-Cardozo, M., Verth, G., & Erdélyi, R. 2012b, in *IAU Symposium*, Vol. 286, *IAU Symposium*, ed. C. H. Mandrini & D. F. Webb, 437–440

Marsh, M. S. & Walsh, R. W. 2009, *ApJ*, 706, L76

Mathioudakis, M., Jess, D. B., & Erdélyi, R. 2013, *Space Sci. Rev.*, 175, 1

McLean, D. J. & Sheridan, K. V. 1973, *Sol. Phys.*, 32, 485

Moreels, M. G., Freij, N., Erdélyi, R., Van Doorsselaere, T., & Verth, G. 2015, *A&A*, 579, A73

Morton, R. J., Erdélyi, R., Jess, D. B., & Mathioudakis, M. 2011, *ApJ*, 729, L18

Morton, R. J., Verth, G., Jess, D. B., Kuridze, D., Ruderman, M. S., Mathioudakis, M., & Erdélyi, R. 2012, *Nature Communications*, 3, 1315

Nakariakov, V. M. & Erdélyi, R. 2009, *Space Sci. Rev.*, 149, 1

Nakariakov, V. M., Hornsey, C., & Melnikov, V. F. 2012, *ApJ*, 761, 134

Nakariakov, V. M. & Melnikov, V. F. 2009, *Space Sci. Rev.*, 149, 119

Nakariakov, V. M. & Ofman, L. 2001, *A&A*, 372, L53

Nakariakov, V. M. & Verwichte, E. 2005, *Living Reviews in Solar Physics*, 2, 3

Ofman, L. & Aschwanden, M. J. 2002, *ApJ*, 576, L153

Ofman, L. & Wang, T. J. 2008, *A&A*, 482, L9

Pascoe, D. J., Nakariakov, V. M., & Arber, T. D. 2007, *Sol. Phys.*, 246, 165

Pascoe, D. J., Nakariakov, V. M., Arber, T. D., & Murawski, K. 2009, *A&A*, 494, 1119

Roberts, B. 2000, *Sol. Phys.*, 193, 139

Roberts, B., Edwin, P. M., & Benz, A. O. 1984, *ApJ*, 279, 857

Rosenberg, H. 1970, *A&A*, 9, 159

Ruderman, M. S. & Erdélyi, R. 2009, *Space Sci. Rev.*, 149, 199

Ruderman, M. S. & Roberts, B. 2002, *ApJ*, 577, 475

Soler, R., Goossens, M., Terradas, J., & Oliver, R. 2013, *ApJ*, 777, 158

—. 2014, *ApJ*, 781, 111

Spruit, H. C. 1982, *Sol. Phys.*, 75, 3

Uchida, Y. 1970, *PASJ*, 22, 341

Van Doorsselaere, T., Andries, J., Poedts, S., & Goossens, M. 2004, *ApJ*, 606, 1223

Van Doorsselaere, T., Wardle, N., Del Zanna, G., Jansari, K., Verwichte, E., & Nakariakov, V. M. 2011, *ApJ*, 727, L32

Vasheghani Farahani, S., Hornsey, C., Van Doorsselaere, T., & Goossens, M. 2014, *ApJ*, 781, 92

Verth, G. & Erdélyi, R. 2008, *A&A*, 486, 1015

Verwichte, E., Van Doorsselaere, T., White, R. S., & Antolin, P. 2013, *A&A*, 552, A138

White, R. S. & Verwichte, E. 2012, *A&A*, 537, A49

Yuan, D., Pascoe, D. J., Nakariakov, V. M., Li, B., & Keppens, R. 2015, *ApJ*, 799, 221

Zaitsev, V. V. & Stepanov, A. V. 1975, *Issledovaniia Geomagnetizmu Aeronomii i Fizike Solntsa*, 37, 3

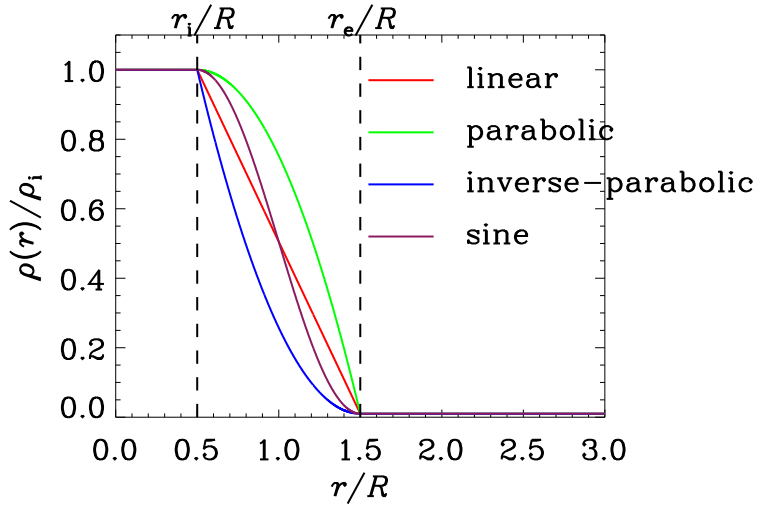


Fig. 1.— Transverse equilibrium density profiles as a function of r . The profiles differ only in how they are described in a transition layer sandwiched between the internal (with a uniform density ρ_i) and external (with a uniform density ρ_e) parts. The transition layer is of width l , and is located between $r_i = R - l/2$ and $r_e = R + l/2$, with R being the cylinder radius. Four different choices of the density profiles in the transition layer are adopted as labeled, and are given by Eq. (4). For illustration purposes, l is chosen to be R , and ρ_i/ρ_e is chosen to be 100.

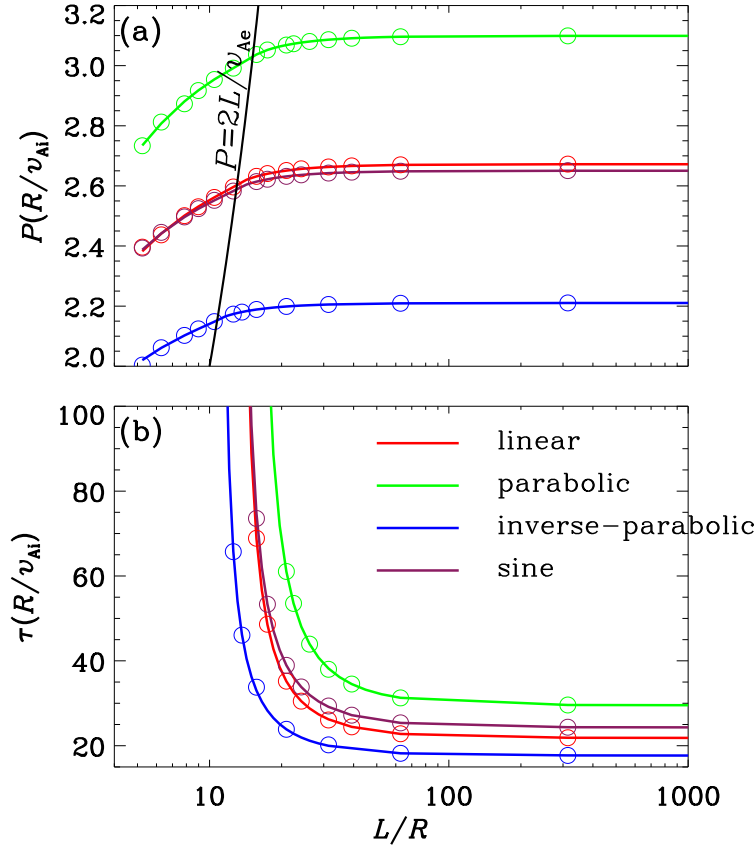


Fig. 2.— (a) Period P and (b) damping time τ as functions of loop length L . Four different choices of density profiles are examined as labeled. The black line in (a) represents $P = 2L/v_{Ae}$ and separates the trapped (to its left) from leaky (right) regimes. The open circles represent the values for P and τ obtained by solving Eq. (19) from an initial-value-problem perspective, which is independent from the eigen-value-problem approach presented in the text. Here the width of the transition layer $l = R$, and the density contrast $\rho_i/\rho_e = 100$.

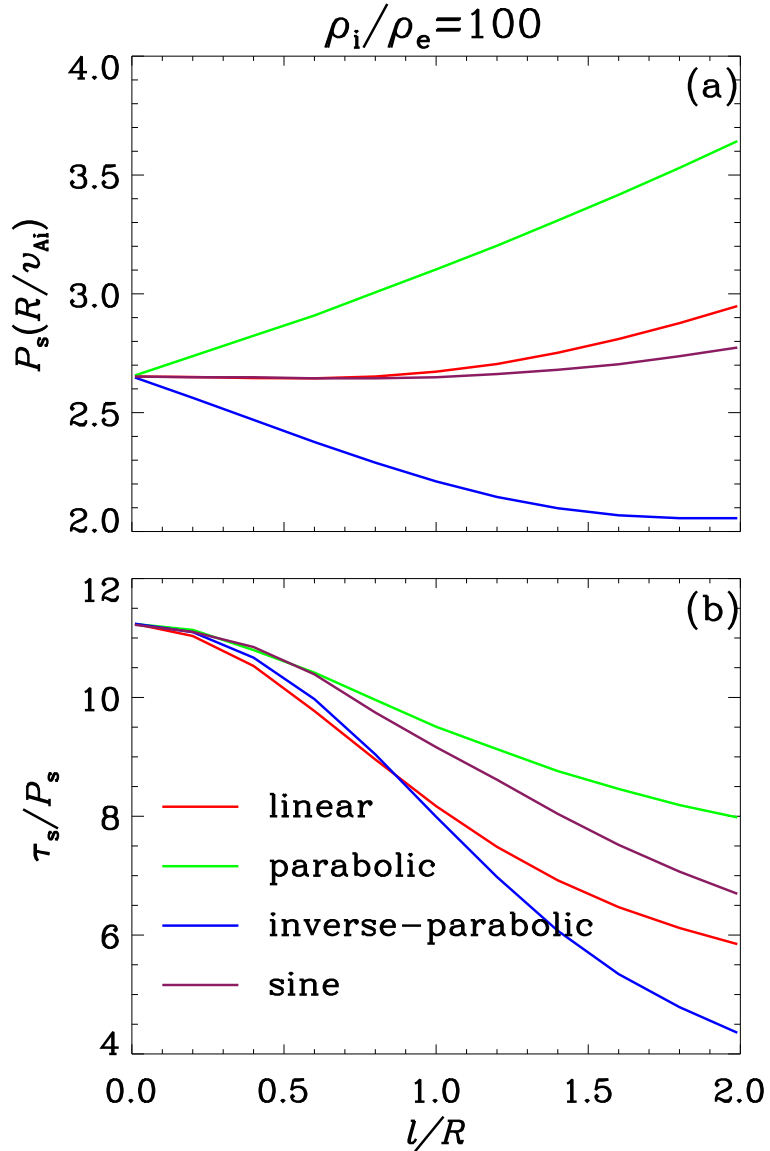


Fig. 3.— Saturation values for (a) period P_s and (b) damping time τ_s as functions of the width of the transition layer l . These saturation values are attained for sufficiently thin loops. Four different choices of the density profiles are examined as labeled. Here the density contrast $\rho_i/\rho_e = 100$.

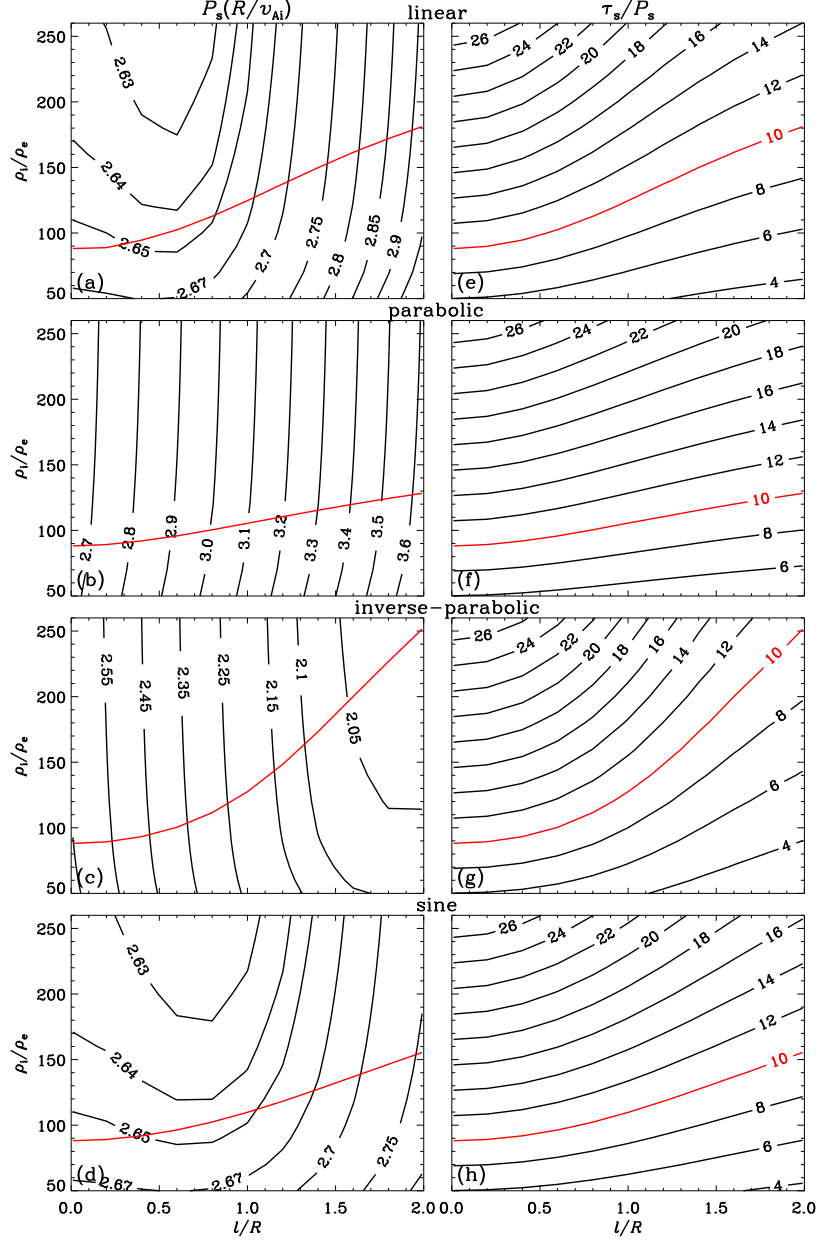


Fig. 4.— Contour plots in the $[l/R, \rho_i/\rho_e]$ space for the saturation values for period P_s (the left column) and damping-time-to-period ratio τ_s/P_s (right). These saturation values are attained for sufficiently thin loops. Each row represents one of the four different choices of the density profiles as labeled. The red curve in each panel represents where $\tau_s/P_s = 10$, corresponding to the event reported in [McLean & Sheridan \(1973\)](#)

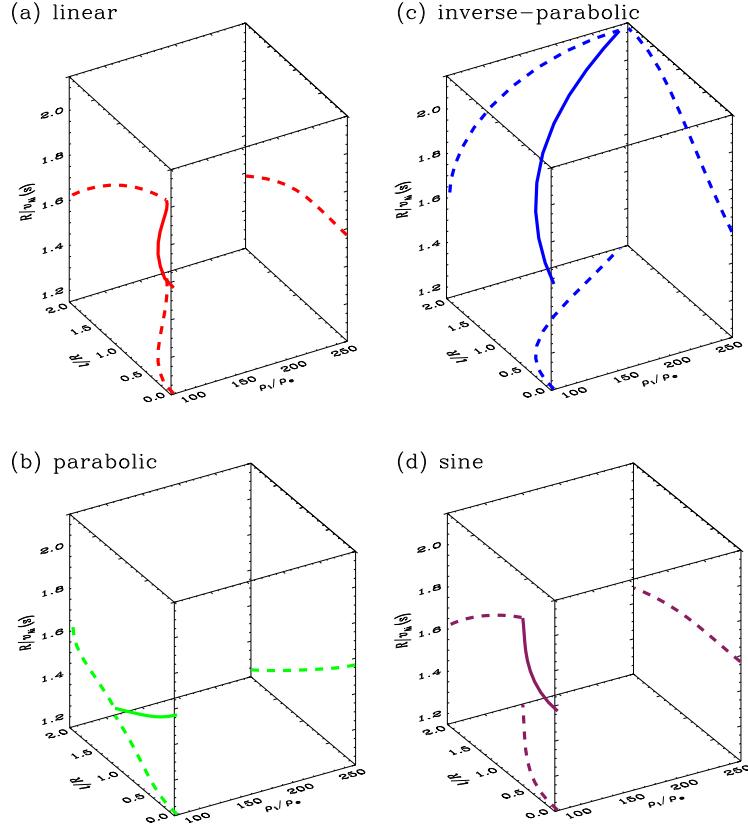


Fig. 5.— Inversion curves (the solid lines) together with their projections (dashed) in the three-dimensional space formed by $[R/v_{Ai}, l/R, \rho_i/\rho_e]$. Four choices for the density profiles are examined and given in different panels as labeled. All points along an inversion curve are equally compatible with the quasi-periodic-pulsation event reported in [McLean & Sheridan \(1973\)](#) where the oscillation period is 4.3 secs, and the damping-time-to-period ratio is 10.

l/R	linear		parabolic		inverse-parabolic		sine	
	ρ_i/ρ_e	R/v_{Ai} (sec)	ρ_i/ρ_e	R/v_{Ai} (sec)	ρ_i/ρ_e	R/v_{Ai} (sec)	ρ_i/ρ_e	R/v_{Ai} (sec)
0.01	88.1	1.62	88.2	1.62	88.1	1.62	88.1	1.62
0.2	88.9	1.62	89.2	1.57	89.3	1.68	89.1	1.62
0.4	94.6	1.63	92	1.52	93.2	1.74	91.9	1.62
0.6	102.4	1.63	95.8	1.48	100.4	1.81	96.4	1.63
0.8	112.75	1.62	100.4	1.43	111.5	1.88	102.4	1.63
1.0	124.7	1.61	105.4	1.39	127.5	1.95	109.8	1.62
1.2	137.4	1.6	110.5	1.35	148.4	2.02	118.2	1.62
1.4	149.8	1.57	115.4	1.3	173.2	2.07	127.4	1.61
1.6	161.5	1.54	120	1.26	200.1	2.1	136.9	1.6
1.8	172	1.51	124.4	1.22	226.8	2.12	146.4	1.58
1.99	181.1	1.47	128.2	1.18	251.4	2.13	155.4	1.56

Table 1: The inverted values for the transverse density length scale in units of loop radius (l/R), density contrast ρ_i/ρ_e and the transverse Alfvén transit time R/v_{Ai} . This inversion is made for the quasi-periodic-pulsation event reported in [McLean & Sheridan \(1973\)](#), assuming that the associated flare loop is sufficiently thin. For this event, the oscillation period is 4.3 secs, and the damping-time-to-period ratio is 10.